Nanoscale

ROYAL SOCIETY OF CHEMISTRY

PAPER

View Article Online
View Journal | View Issue

Check for updates

Cite this: *Nanoscale*, 2025, **17**, 10901

Synthesis and electronic structure of atomically thin 2H-MoTe$_2$†

Wenjuan Zhao, *‡[a,b,c] Xieyu Zhou,‡[d] Dayu Yan,‡[a,b] Yuan Huang,*[a,e] Cong Li,[a,b] Qiang Gao,[a,b] Paolo Moras, [c] Polina M. Sheverdyaeva, [c] Hongtao Rong,[a,b] Yongqing Cai,[a,b] Eike F. Schwier,[f] Xixia Zhang,[g] Cheng Shen,[a,b] Yang Wang,[a,b] Yu Xu,[a,b] Wei Ji, [d] Chen Liu,[h] Youguo Shi,[a] Lin Zhao,[a] Lihong Bao, [a] Qingyan Wang,[a] Kenya Shimada, [f] Xutang Tao, [g] Guangyu Zhang,[a,b] Hongjun Gao, [a,b] Zuyan Xu,[i] Xingjiang Zhou*[a,b,j,k] and Guodong Liu *[a,b,j]

An in-depth understanding of the electronic structure of 2H-MoTe$_2$ at the atomic layer limit is a crucial step towards its exploitation in nanoscale devices. Here, we show that millimeter-sized monolayer (ML) MoTe$_2$ samples, as well as smaller sized bilayer (BL) samples, can be obtained using the mechanical exfoliation technique. The electronic structure of these materials is investigated by angle-resolved photoemission spectroscopy (ARPES) for the first time and by density functional theory (DFT) calculations. The comparison between experiments and theory allows us to describe ML MoTe$_2$ as a semiconductor with a direct gap at the K point. This scenario is reinforced by the experimental observation of the conduction band minimum at K in Rb-doped ML MoTe$_2$, resulting in a gap of at least 0.924 eV. In the BL MoTe$_2$ system, the maxima of the bands at Γ and K show very similar energies, thus leaving the door open to a direct gap scenario, in analogy to WSe$_2$. The monotonic increase in the separation between spin-split bands at K while moving from ML to BL and bulk-like MoTe$_2$ is attributed to interlayer coupling. Our findings can be considered as a reference to understand quantum anomalous and fractional quantum anomalous Hall effects recently discovered in ML and BL MoTe$_2$ based moiré heterostructures.

Received 9th December 2024,
Accepted 18th March 2025

DOI: 10.1039/d4nr05191b

rsc.li/nanoscale

1 Introduction

Monolayer transition metal dichalcogenides (TMDCs) with the formula MX$_2$ (where M = Mo and W; X = S, Se, and Te) and 2H phase exhibit unique and remarkable properties, including direct band gap transition,[1–4] well-defined valley degrees of freedom and spin-valley locking,[5] huge exciton binding energy,[6,7] and Ising superconductivity.[8] Their unique properties can lead to numerous applications in next-generation nanoelectronics,[9] optoelectronics,[10] and valleytronics.[7]

MoTe$_2$ is a small gap semiconductor hosting exotic and prominent quantum phenomena in the few layer limit.[11–13] Recently, the quantum anomalous Hall effect (QAH, also referred to as the integer Chern insulating state) has been reported in twisted bilayer (BL) MoTe$_2$ [13] and in AB-stacked MoTe$_2$/WSe$_2$ moiré hetero-BLs.[12] The long-sought-after fractional quantum anomalous Hall effect (FQAH, also called the fractional Chern insulating state) has been discovered only in twisted BL MoTe$_2$,[13–16] although it had been predicted in some twisted TMDC moiré BLs.[12,17–19] Thus, the rhombohedrally stacked twisted MoTe$_2$-based BLs have emerged as a promising platform for investigating both QAH and FQAH effects at zero magnetic field. Additionally, a giant intrinsic spin Hall effect

---

[a] Beijing National Laboratory for Condensed Matter Physics, Institute of Physics, Chinese Academy of Sciences, Beijing 100190, China.
E-mail: Wenjuan.Zhao@trieste.ism.cnr.it, yhuang01@iphy.ac.cn, XJZhou@iphy.ac.cn, gdliu_arpes@iphy.ac.cn
[b] University of Chinese Academy of Sciences, Beijing 100049, China
[c] CNR-Istituto di Struttura della Materia (CNR-ISM), SS 14, Km 163, 5, 34149 Trieste, Italy
[d] Department of Physics, Renmin University of China, Beijing 100872, P.R. China
[e] School of Physics, School of Integrated Circuits and Electronics, Beijing Institute of Technology, Advanced Research Institute of Multidisciplinary Sciences, Beijing 100081, China
[f] Research Institute for Synchrotron Radiation Science (HiSOR), Hiroshima University, Higashi-Hiroshima, Hiroshima 739-0046, Japan
[g] State Key Laboratory of Crystal Materials, Shandong University, 250100 Jinan, Shandong, China
[h] Institute of High Energy Physics, Chinese Academy of Sciences, Beijing 100049, China
[i] Technical Institute of Physics and Chemistry, Chinese Academy of Sciences, Beijing 100190, China
[j] Songshan Lake Materials Laboratory, Dongguan 523808, China
[k] Beijing Academy of Quantum Information Sciences, Beijing 100193, China

† Electronic supplementary information (ESI) available. See DOI: **https://doi.org/10.1039/d4nr05191b**

‡ These people contributed equally to the present work.

has also been found in AB-stacked $MoTe_2/WSe_2$ moiré BLs.[20–22] These findings pay the way for investigating novel physical properties such as fractional charge excitation and anyon statistics under zero magnetic field conditions, thus providing new opportunities for dissipationless transport, topological quantum computing and spintronics.[13–16,20,23] In spite of the importance of $MoTe_2$, there have been no reports on the electronic band structures of monolayer (ML) $MoTe_2$, which is the ultimate building block of the moiré heterostructures mentioned above.

Compared to the molecular beam epitaxy growth method,[24] mechanical exfoliation is a simpler and more universal technique. It typically results in weaker substrate interactions and yields higher quality samples.[25] In this paper, we report on the synthesis of millimeter-sized ML $MoTe_2$ samples *via* the mechanical exfoliation method. The superior structural uniformity of the so-obtained layers allows us to perform detailed characterization of their properties by space-averaging techniques, such as low-energy electron diffraction (LEED), Raman spectroscopy and, for the first time, angle-resolved photoemission spectroscopy (ARPES). The electronic structure of ML $MoTe_2$ displays a flat state around Γ and a valence band maximum (VBM) at the K point, which are well reproduced by density functional theory (DFT) calculations. On the basis of this agreement, the system can be described as a semiconductor with a direct gap at the K point. The observation of conduction band filling at K in Rb-doped ML $MoTe_2$ strengthens this scenario. Occasionally, mechanical exfoliation gives rise to well-ordered patches of BL $MoTe_2$ surrounded by areas of ML and multilayer (bulk-like) $MoTe_2$. The topmost occupied states at Γ and K in these BLs exhibit similar binding energy. This may suggest that BL $MoTe_2$ is a direct gap semiconductor, in analogy to BL WSe_2.[26] Finally, we discover that the energy separation of the spin-split states at K increases monotonically from ML to BL and to multilayer $MoTe_2$ as a consequence of interlayer coupling. Our work sheds light on the electronic structure of atomically thin $MoTe_2$ layers, thus providing fundamental support to understand the origin of QAH and FQAH effects occurring in $MoTe_2$-based heterostructures.

2. Methods

ML, BL and multilayer (bulk-like) $MoTe_2$ flakes were prepared by the mechanical exfoliation method from bulk crystals, as illustrated in Fig. 1(a).[25] ARPES measurements on ML and multilayer (more than 10 MLs) samples were performed with a photon energy of 21.218 eV, using a home-built photoemission spectroscopy system[27] equipped with a VUV5000 helium lamp (spot size: 0.8 mm × 0.8 mm) and a DA30L electron energy analyzer (Scienta Omicron). The overall energy resolution was set to 20 meV, and the angular resolution to 0.2°. ARPES data of BL samples were collected at the BL-1 end station of HiSOR with a photon energy of 45 eV (spot size: 0.8 mm × 0.3 mm). All the samples were measured at 30–40 K under a base pressure better than 5×10^{-11} mbar, after mild vacuum annealing at about 500 K.

DFT calculations were performed using the generalized gradient approximation and the projector augmented wave method[28,29] as implemented in the Vienna *ab initio* simulation package (VASP).[30,31] A uniform Monkhorst–Pack k mesh of $21 \times 21 \times 5$ was adopted for integration over the Brillouin zone of bulk $MoTe_2$, and a mesh of $21 \times 21 \times 1$ was used for ML and BL $MoTe_2$. A plane-wave cutoff energy of 700 eV was used for structural relaxation and electronic structure calculations. A distance of more than 15 Å along the out-of-plane direction was adopted to eliminate interaction between adjacent layers. Dispersion correction was made using the van der Waals Density Functional (vdW-DF) approach,[32–34] with the optB86b functional for the exchange potential, which was proved to be accurate in describing the structural properties of layered materials[35–40] and was adopted for structure related calculations. All atoms were allowed to relax until the residual force per atom was less than 0.01 eV $Å^{-1}$. In our electronic structure calculations, we used the Perdew–Burke–Ernzerhof (PBE)[41] functional with consideration of spin–orbit coupling (SOC), based on the vdW-DF optimized atomic structures. A plane-wave cutoff energy of 500 eV and a k mesh of $9 \times 9 \times 3$ were used for energy calculations for bulk $MoTe_2$ ($9 \times 9 \times 1$ for ML and BL).

3 Results and discussion

Fig. 1(a) illustrates the sample preparation procedure of atomically thin $MoTe_2$ samples by the mechanical exfoliation method.[25] The SiO_2/Si substrate (black rectangle) is cleaned using oxygen plasma, covered with a 3–20 nm thick layer of gold (yellow rectangle) and cleaned again using oxygen plasma and ultrasonication. Adhesive tape (blue rectangle) loaded with a bulk $MoTe_2$ layer (green rectangle) is brought into contact with the substrate and then removed to complete the exfoliation process. Fig. 1(b–e) show the characterization of samples prepared according to this procedure. Typically, optical microscopy images (Fig. 1(b)) reveal the presence of millimeter-sized $MoTe_2$ domains (pink areas) covering most of the substrate (dark pink areas). After mild annealing (500 K) under ultra-high vacuum conditions, a sharp hexagonal LEED pattern becomes visible (Fig. 1(c)), thus indicating the long-range order of the $MoTe_2$ domains. In order to determine the vibrational properties of these domains, Fig. 1(d) compares the Raman data acquired on the pink area shown in Fig. 1(b) (red spectrum) and on bulk-like (more than 10 MLs) $MoTe_2$ (blue spectrum) with a laser wavelength of 532 nm. In the blue spectrum, the A_{1g} mode is located at 173.67 cm^{-1} and the $E_{2g}{}^1$ mode at 233.87 cm^{-1}, while in the red spectrum they are found at 170.58 cm^{-1} and 235.92 cm^{-1}, respectively (insets in Fig. 1(d)). These shifts from the reference bulk-like values are consistent with previously reported results for ML $MoTe_2$.[42] The topmost atomic force microscopy (AFM) image in Fig. 1(e) directly shows that the height difference between the substrate and the millimeter-sized $MoTe_2$ domains is 5.97 ± 1 Å (red line

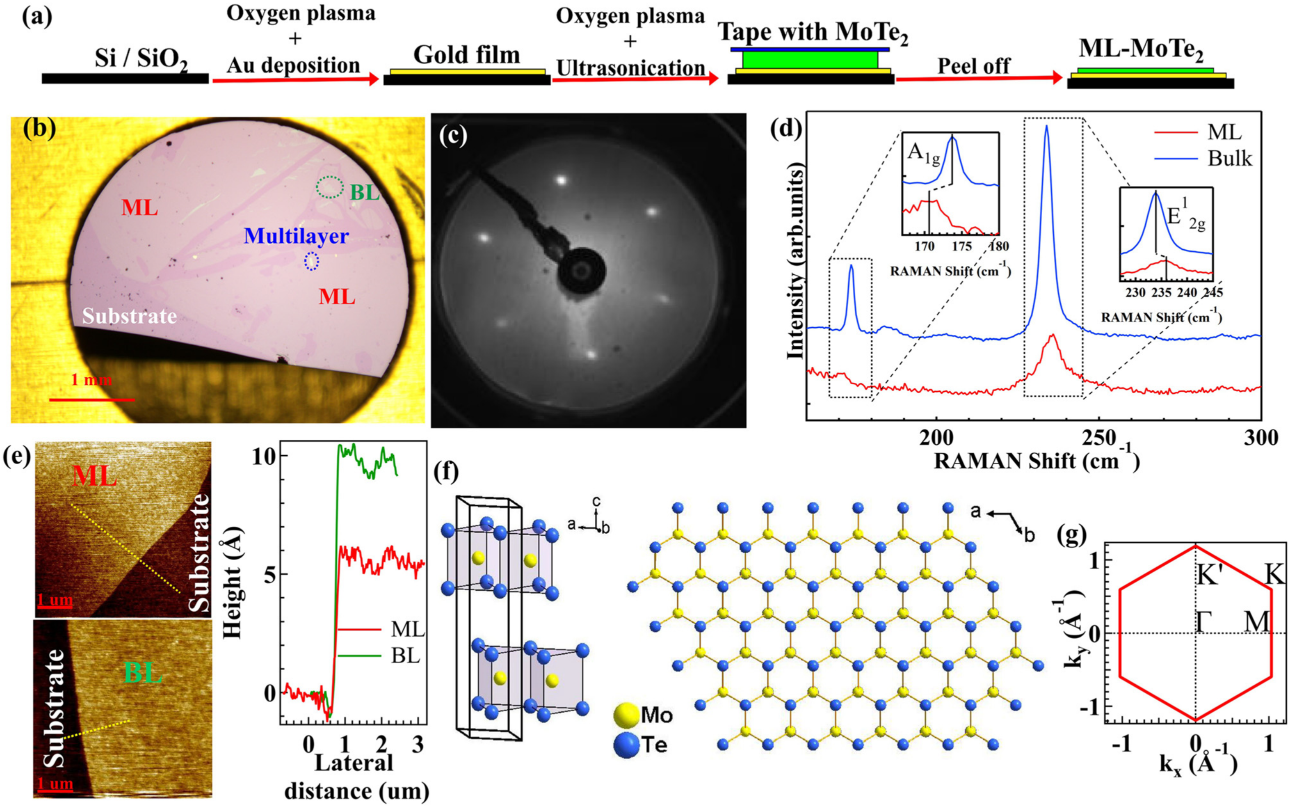

Fig. 1 (a) Cartoon illustrating the sample fabrication process. Black, yellow, green, and blue rectangular bars represent the SiO_2/Si wafer, gold film, $MoTe_2$ layer, and adhesive tape, respectively. (b) Typical optical microscopy image of a sample after mechanical exfoliation of $MoTe_2$. The predominant pink areas are millimeter-sized domains of ML $MoTe_2$ in contact with the substrate (dark pink areas). Small light pink and white areas surrounded by dotted ovals represent BL and multilayer $MoTe_2$, respectively. (c) LEED pattern taken on a sample with prevalent ML $MoTe_2$ coverage. (d) Raman spectra of ML (red) and bulk (blue) $MoTe_2$. Characteristic peaks are highlighted in the insets. (e) AFM images taken at the edge between the Au substrate and ML (top panel) and BL (bottom panel) $MoTe_2$ domains. The thickness profiles extracted from the lines shown in the AFM images are compared in the right panel. (f) Crystal structure of $MoTe_2$ in isometric and top views. (g) SBZ of $MoTe_2$.

in the right panel), which is in the range of the expected thickness of ML $MoTe_2$ (6.98 Å). Overall, these experimental data allow us to identify the pink areas of Fig. 1(b) as well-ordered domains of ML $MoTe_2$.

Fig. 1(b) also displays small regions (typical size in the order of 0.1 mm) with light pink and white optical contrast. The AFM analysis of the light pink areas (bottommost image in Fig. 1(e)) shows that their height with respect to the substrate corresponds to 10.32 ± 1 Å, *i.e.* nearly twice the measured thickness of ML $MoTe_2$. Therefore, these areas are identified as domains of BL $MoTe_2$. Finally, the white areas are bulk-like multilayers of $MoTe_2$. Occasionally, the mechanical exfoliation method produces millimeter sized areas of BL and multilayer (from here onwards called bulk) $MoTe_2$, which allow space-averaging ARPES analysis, as shown in Fig. 2. Fig. S1 in the ESI†[43] shows the structural characterization of a sample with BL domains on the order of 1 mm^2, where the thickness of the BL areas is measured by AFM and confirmed by cross-sectional transmission electron microscopy.

For reference, Fig. 1(f) displays the crystal structure of 2H-$MoTe_2$, which comprises van der Waals Te–Mo–Te trilayers (left panel) stacked along the *c*-axis and forming a honeycomb lattice in the (0001) projection plane (right panel). The prisms of adjacent trilayers point in opposite directions within the plane. Among the TMDCs, $MoTe_2$ possesses notably large lattice parameters (a = 3.52 Å and c = 13.97 Å).[44] Fig. 1(g) presents the surface Brillouin zone (SBZ) of $MoTe_2$, along with high symmetry points, which will be useful for the discussion of the ARPES data.

Fig. 2 reports an overview of the ARPES analysis along the M–Γ–K–M path for ML (Fig. 2(a and d)) and BL (Fig. 2(b and e)) taken on a millimeter sized domain of the sample shown in Fig. S1† and bulk (Fig. 2(c and f)) $MoTe_2$. The spectra are shown as acquired in the top row and after second derivative treatment (along the energy axis) in the bottom row, to enhance the sensitivity to weak electronic features. The well-defined Fermi level (E_F) observed in the second derivative data derives from the partially uncovered Au layer in the substrate. The calculated band structures (red dotted lines) are overlaid on the data in the bottom row of the figure (see Fig. S2 in the ESI† for calculations extended above E_F [43]).

In the ML sample (Fig. 2(a and d)), the topmost band observed near Γ is very flat and mainly derives from Mo d_{z^2} orbitals, with a minor Te p_z contribution, which exhibits sig-

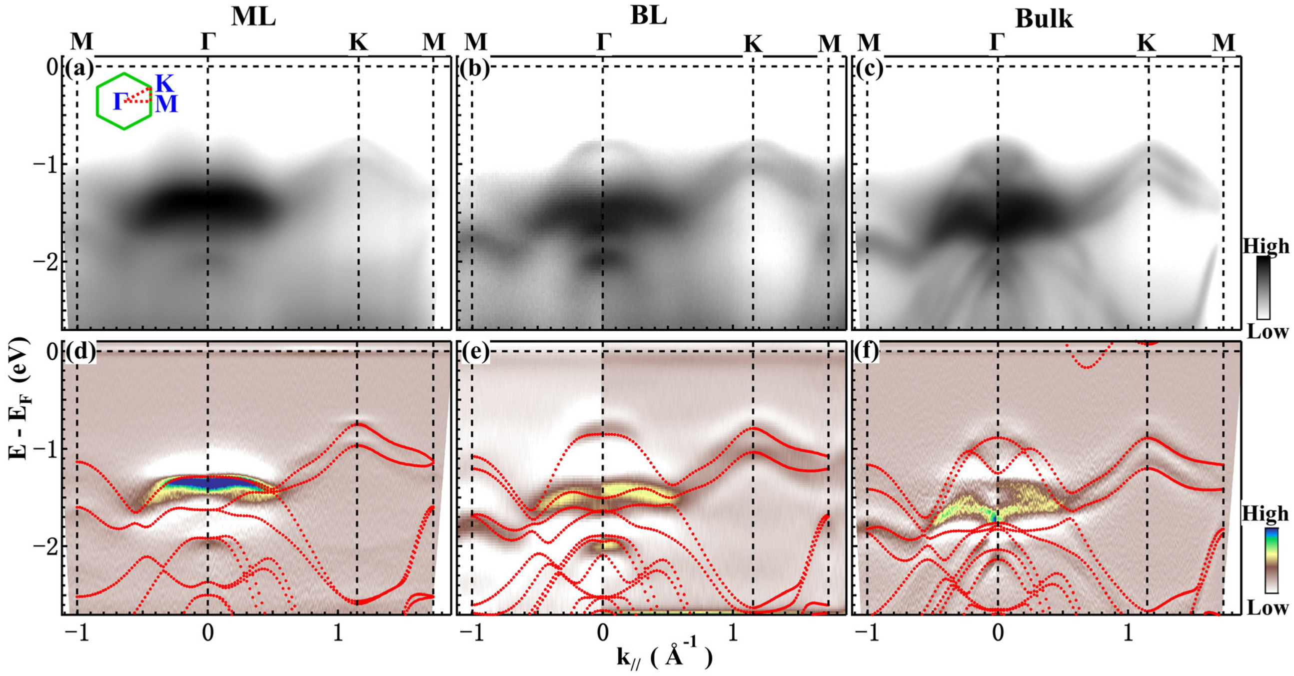

Fig. 2 (a–c) ARPES maps illustrating the electronic band structures along the M–Γ–K–M high symmetry direction in ML (a), BL (b), and bulk (c) $MoTe_2$, as indicated at the top. The inset in (a) shows the high symmetry directions (red dashed lines) in the SBZ (green hexagon). The lower panels (d–f) depict the second derivative plots of panels (a–c), respectively. The red dotted curves overlaid on the plots represent the corresponding bands calculated by DFT.

nificant localization in the lattice plane (calculations of the orbital character are reported in Fig. S3 in the ESI†[43]). The two parabolic-like bands with maxima at the K point primarily derive from in-plane delocalized Mo $d_{x^2-y^2}/d_{xy}$ orbitals, with a small contribution from Te p_x/p_y orbitals. These bands form a spin–split pair, originating from the strong SOC of Mo atoms and the absence of structural inversion symmetry, and become degenerate along the Γ–M direction due to time-reversal symmetry. The VBM is found at K (−0.76 eV), which lies well above the topmost state at Γ (−1.375 eV) (see also Fig. S4 in the ESI†). The observations of a flat band at Γ and the VBM at K are consistent with those of other ML-MX_2 materials.[26,45–47] In addition to these characteristic features, two parabolic bands centered at the M point with energies ∼−1.25 eV and −1.7 eV, as well as another parabolic band centered at the Γ point around −2 eV, are discernible. The increasing background below −2 eV in Fig. 2(a and d) originates from the intense 5d states of the underlying polycrystalline gold substrate. The experimental band structure of the ML $MoTe_2$ sample within the first 2 eV below E_F turns out to be well reproduced by the calculations (Fig. 2(d)). This good correspondence allows us to describe ML $MoTe_2$ as a direct band gap semiconductor.

Fig. 3 presents further data supporting the direct band gap scenario in ML $MoTe_2$. To directly determine the momentum position of the conduction band minimum (CBM), Rb atoms are evaporated on the surface of ML $MoTe_2$ to partially fill its unoccupied bands.[48] The changes induced by Rb deposition in the band structure of ML $MoTe_2$ along the Γ–K direction are shown in Fig. 3(a–d). As the amount of deposited Rb increases, the bands shift continuously away from E_F (Fig. 3(b–d)). At the highest Rb coverage (Fig. 3(d)), the VBM and the topmost state at Γ are located at −0.96 and −1.66 eV. The detailed evolution of the bands at the Γ and K points is depicted through the energy distribution curves (EDCs) taken at the $k_{||}$ positions marked by the orange dashed lines in Fig. 3(a) and illustrated in Fig. 3(e) and (f), respectively. These EDCs demonstrate a peak shift of 0.285 eV at the Γ point and 0.2 eV at the K point. These data indicate a non-rigid band shift that could be used for electronic structure engineering of ML $MoTe_2$.

Interestingly, the spectra acquired in the proximity of K′ (cut 2 in the inset of Fig. 3(a)) for the highest Rb deposition display a peak near E_F (inset in Fig. 3(g)). The emergence of this feature can be observed in Fig. 3(h), which shows the EDCs extracted at K′ for both pristine (red) and highly Rb doped $MoTe_2$ (green). The peak is identified as the CBM at the K′ point. Together with the VBM at the K/K′ point, this new state proves the existence of a direct gap of at least 0.924 eV. This gap value is different from that of pristine $MoTe_2$ because of band renormalization effects, which clearly manifest in the non-rigid Rb-induced band shifts. However, it is close to the gap size expected from the DFT calculation (0.97 eV, Fig. S3†). This observation is in line with other band calculations,[43,49,50] photoluminescence[49,51,52] and STS[24] measurements for ML $MoTe_2$.

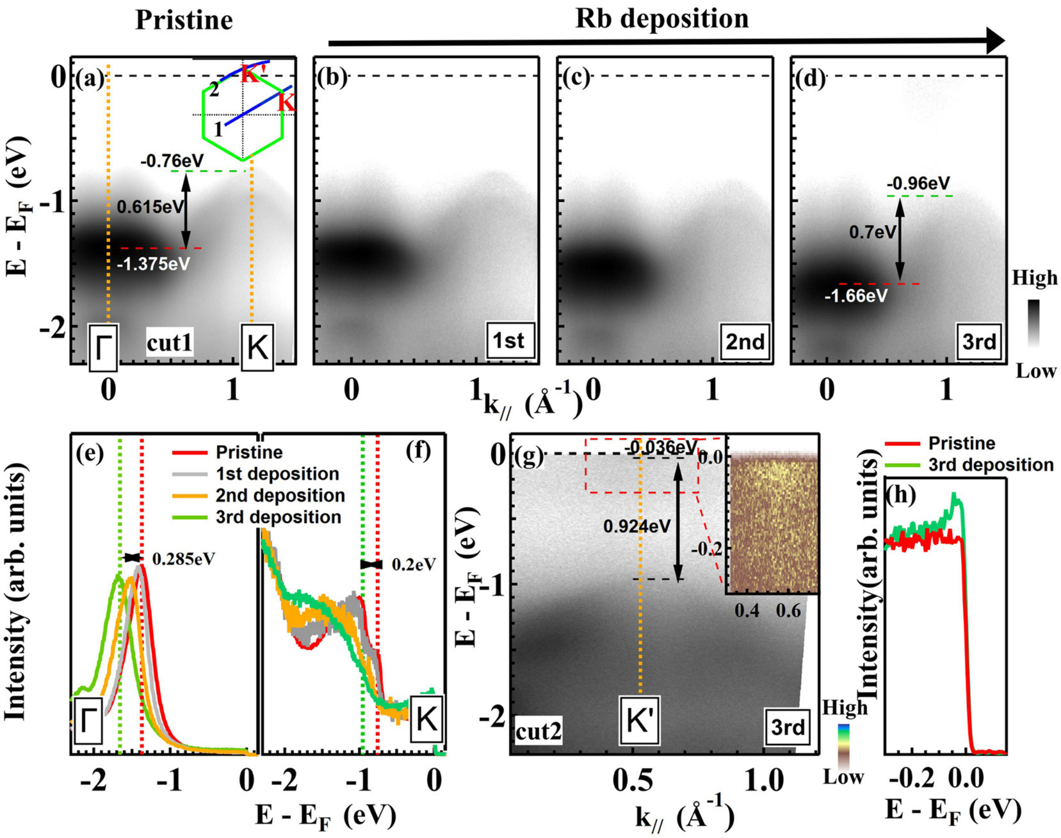

Fig. 3 Direct band gap observation in ML $MoTe_2$ through Rb deposition. ARPES data of (a) pristine and (b–d) Rb-doped $MoTe_2$ ML measured along cut 1 (Γ–K direction) as shown in the inset of panel (a). (e and f) EDCs at the Γ and K points extracted from panels (a–d), respectively. The red and green dashed lines mark the positions of the band maxima for the pristine $MoTe_2$ sample and after the 3rd Rb deposition. (g) ARPES data along cut 2 after the 3rd Rb deposition, where a new band appears near E_F at K′ (see the inset). (h) EDCs at K′ for pristine $MoTe_2$ (red) and after the 3rd Rb deposition (green).

BL and bulk $MoTe_2$ exhibit electronic bands similar to those of the ML case with differences mainly concentrated around the Γ point. In Fig. 2(b and e), an additional parabolic band is present above the flat band. In Fig. 2(c and f), a complex packed structure of parabolic bands is observed above the flat band, which is consistent with the reported results for more than 3 ML thick $MoTe_2$ samples.[11,48] The orbital calculation in Fig. S3†[43] indicates that the parabolic band (BL) and the packet of bands (bulk) can be explained by the repulsion between Mo d_{z^2} and Te p_z orbitals perpendicular to the plane. This repulsion increases the energy at Γ in BL and bulk $MoTe_2$ and reduces the energy from Γ to M and Γ to K because of the increasing component of in-plane orbitals. Below the flat band, the parabolic bands become clearer in BL and bulk $MoTe_2$ samples.

It is worth noting that the topmost valence states of BL $MoTe_2$ at both Γ and K are located at −0.795 eV (a detailed comparison is provided in Fig. S5 in the ESI†[43]). This situation is analogous to that observed in BL WSe_2, which is predicted to be a direct gap semiconductor,[26,53,54] but contrasts with most indirect-gap BL TMDC semiconductors, such as MoS_2, WS_2, and $MoSe_2$, where the VBM is found at Γ.[45,53,55–57] Our ARPES data may suggest the presence of a direct gap at K in BL $MoTe_2$, which would be consistent with the results of low-temperature photoluminescence experiments.[51,58,59] However, our calculations (Fig. S2†[43]) reveal that the CBM is located halfway between Γ and K. This inconsistency can be attributed to the slight lattice mismatch between the calculated free-standing BL and the real BL $MoTe_2$ on the Au substrate, which was not considered in our calculations.[60,61] ARPES is inherently unable to directly observe the conduction band due to the lack of electron occupation, thus precluding the verification of the CBM position through this method. Further investigation is required to clarify the nature (direct *vs.* indirect gap semiconductor) of BL $MoTe_2$.

For bulk $MoTe_2$, the topmost valence state at the Γ point (−0.665 eV) is closer to E_F than that at K (−0.87 eV), thus indicating a typical indirect gap semiconductor behavior. Overall, the valence band structures in Fig. 2 provide clear evidence for the indirect-to-direct band gap transition with decreasing layer thickness from bulk (indirect gap) to ML (direct gap). This transition originates from the quantum confinement effect[2,62] and is consistent with reported photoluminescence results.[49,51,52,63]

The splitting of the valence bands (VB1 and VB2) near the K point holds significance for various crucial phenomena and properties of MX_2 materials, including spin-valley locking, the AB exciton effect,[6,7] and spin-layer locking.[64] In Fig. 4, we show ARPES data along the Γ–K direction for ML, BL and bulk samples (Fig. 4(a–c)) and the corresponding second derivative plots (Fig. 4(d–f)). To facilitate a quantitative comparison, Fig. 4(g–i) display EDCs at the K point for the different samples. The measured splitting at K increases monotonically with thickness (details of the Gaussian fitting are given in Fig. S6†[43]): 0.212 eV in ML, 0.225 eV in BL and 0.252 eV in bulk $MoTe_2$. These data are consistent with the trend of the DFT results, which give 0.22, 0.24, and 0.31 eV for the respective systems. Generally, in the family of MX_2 TMDCs, the valence band splitting around the K point arises from SOC, inversion symmetry breaking, and interlayer coupling.[5] The increasing splitting size can be attributed to a variation of the interlayer coupling strengths between BL or bulk (Fig. S7†[43]) and ML $MoTe_2$.[5,65] Therefore, our observations imply an interlayer interaction strength in the order of 10 meV and 40 meV for BL and bulk $MoTe_2$, respectively. The increased interlayer coupling strength from BL to bulk is likely to be a consequence of the reduced layer separation as the number of layers increases, thereby enhancing interlayer hopping and coupling.[65]

The splitting of spin-polarized bands is a distinctive feature of ML-TMDCs, resulting from the interplay of SOC and the breaking of inversion symmetry.[5,66,67] The splitting in ML $MoSe_2$ is ~0.18 eV (ref. 45) and in ML MoS_2 is ~0.15 eV.[46] The larger splitting that we observed in ML $MoTe_2$ is a consequence of the larger SOC of Te with respect to Se and S. This characteristic makes ML $MoTe_2$ particularly well-suited for applications in spintronics.

To summarize our results in a quantitative way, we have compiled Table 1 with the relevant parameters of the band structures for the different $MoTe_2$ systems derived from ARPES measurements and DFT calculations. Regarding the K splitting, the difference between the VBM at the K and Γ points, and the size of the direct band gap in ML $MoTe_2$, our calculations show consistent results with the ARPES measurements as discussed above. We have also derived the effective mass near the VBM at both K and Γ points along the Γ–K direction (details in Table S1†[43]). While going from ML to BL and bulk, the observed effective mass at K shows similar values for the different layered samples. Conversely, at Γ, both the observed and calculated hole effective masses for the top of the valence

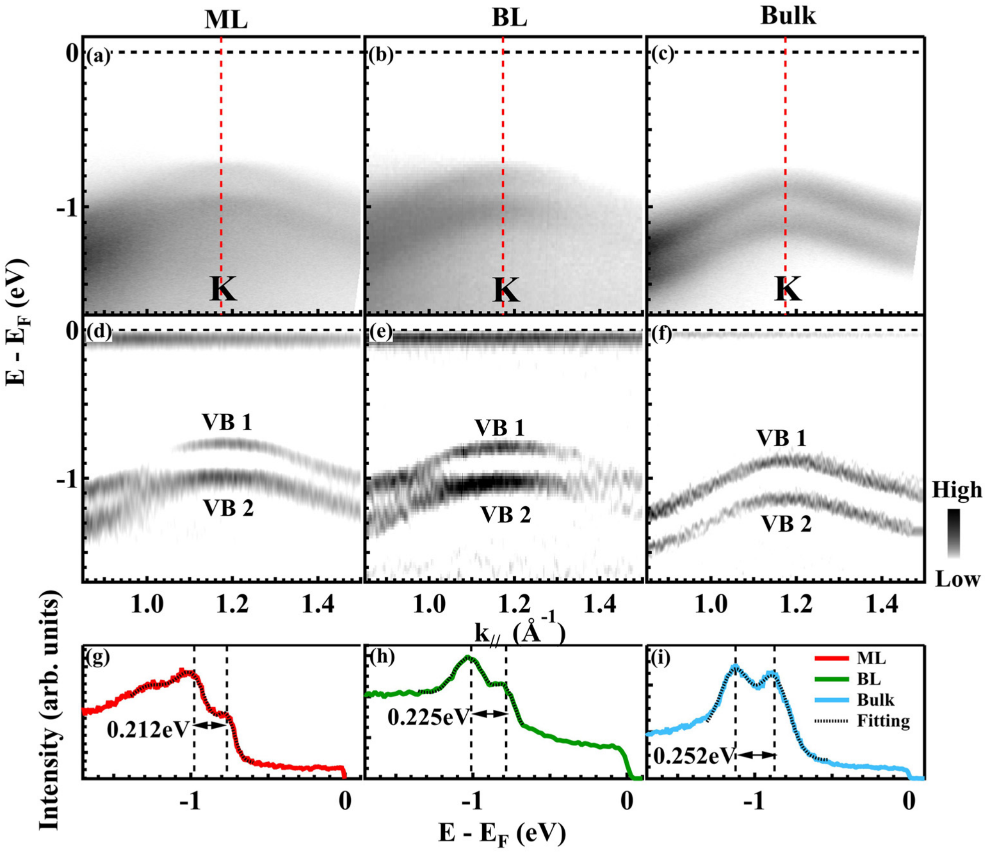

Fig. 4 Layer dependent band splitting at K. (a–c) ARPES maps showing the valence band splitting around K along the Γ–K–M direction for ML, BL and bulk $MoTe_2$, respectively. (d–f) Second derivative spectra of (a–c) along the energy axis, respectively. (g–i) EDCs at K from (a–c), shown as red (ML), green (BL) and blue (bulk) curves, respectively. The black dotted curves are the corresponding Gaussian fitting results, with peak positions indicated by black dashed lines.

Table 1 Electronic parameters extracted from ARPES data and DFT calculations of ML, BL and bulk $MoTe_2$

	ML		BL		Bulk	
Thickness	ARPES	Calculation	ARPES	Calculation	ARPES	Calculation
Splitting at K [eV]	0.212	0.22	0.225	0.24	0.252	0.31
Energy difference between VBM at K and Γ [eV]	0.615	0.536	0	0.059	−0.205	−0.005
Gap size [eV]	0.924[a]	0.97	—	0.91	—	0.72
Effective mass at K [m_0]	1.17	0.59	1.69	0.62	1.56	0.61
Effective mass at Γ [m_0]	13.09	34.52	5	8.5	—	1.27

[a] The value extracted from the ML sample after Rb deposition. m_0 is the electron mass

band exhibit a rapid and monotonic decrease as the number of layers increases. The discrepancy between the experimental ($13.09m_0$) and calculated ($34.52m_0$) effective masses at the Γ point for ML $MoTe_2$ primarily arises from hybridization between the $MoTe_2$ and Au states. Our DFT calculations were performed for free-standing $MoTe_2$ layers. Therefore, the interaction with the substrate is not taken into account. The effective mass of the Au sp states (<1 electron mass[68]) is much lower than that of ML $MoTe_2$. As a result of the $MoTe_2$–Au interaction, the measured effective mass is lower than the calculated one. A similar effect has been reported in the case of ML MoS_2.[69] Importantly, all ARPES analyses and DFT calculations are consistent.

4. Conclusions

In summary, we report on the synthesis of millimeter-sized ML $MoTe_2$ domains using the mechanical exfoliation method. The exceptional structural uniformity of these layers allows for comprehensive characterization using space-averaging techniques. Our investigation reveals that the electronic structure of ML $MoTe_2$ features a flat band around the Γ point and a VBM at the K point, in agreement with DFT calculations. This strongly suggests that the material can be described as a semiconductor with a direct band gap at K. The observation of conduction band filling at K in Rb-doped ML $MoTe_2$, with a direct band gap of at least 0.924 eV, further supports this interpretation. The topmost occupied states of BL $MoTe_2$ at Γ and K exhibit similar binding energies. This opens the possibility that BL $MoTe_2$ is a direct gap system, akin to WSe_2. Finally, the energy separation of the spin-split bands at K increases monotonically from ML to BL to bulk $MoTe_2$ due to interlayer coupling. The present work sheds light on the electronic structure of atomically thin $MoTe_2$ layers, which could be significant in clarifying the origin of quantum anomalous Hall (QAH) and fractional quantum anomalous Hall (FQAH) effects observed in $MoTe_2$-based heterostructures.

Author contributions

W.Z., Xie. Z. and D.Y. contributed equally to this work. G.L., Xin. Z. and W.Z. conceptualized the work; W.Z., Q.G., H.R., E. F.S., Y.W., L.Z., K.S. and G.L. conducted the ARPES experiments; C. L., Y.C., Y.X., L.B. and Z.X. provided instrumental support for the ARPES measurements; W.Z., G.L., P.M. and P. M.S. wrote the article with contributions from all coauthors; D.Y., Y.H., Xix. Z., C.S., C.L., Y.S., Q.W., X.T., G.Z., and H.G. prepared the samples and performed the Raman, AFM and XPS measurements; Xie. Z. and W.J. conducted the DFT calculations; Y.H., G.L. and Xin. Z. supported the network. W.Z., Y. H., Xin. Z. and G.L. are the corresponding authors.

Data availability

The data supporting this article have been included as part of the ESI.†[43]

Conflicts of interest

There are no conflicts to declare.

Acknowledgements

This work is supported by the National Key Research and Development Program of China (No. 2022YFA1403901, 2019YFA0308000 and 2018YFA0704201), the National Natural Science Foundation of China (No. 11574367 and 11874405), and the Youth Innovation Promotion Association of Chinese Academy of Sciences (No. 2017013 and 2019007). PM and PMS acknowledge partial funding through the project EUROFEL-ROADMAP ESFRI of the Italian Ministry of University and Research. Synchrotron ARPES measurements were performed under the approval of the Program Advisory Committee of HiSOR (proposal numbers: 17BU004, 17BU005 and 18AU001).

References

1 J. K. Ellis, M. J. Lucero and G. E. Scuseria, *Appl. Phys. Lett.*, 2011, **99**, 261908.
2 Z. Y. Zhu, Y. C. Cheng and U. Schwingenschlögl, *Phys. Rev. B:Condens. Matter Mater. Phys.*, 2011, **84**, 153402.

3 T. Cheiwchanchamnangij and W. R. L. Lambrecht, *Phys. Rev. B:Condens. Matter Mater. Phys.*, 2012, **85**, 205302.

4 A. Kumar and P. K. Ahluwalia, *Eur. Phys. J. B*, 2012, **85**, 186.

5 D. Xiao, G.-B. Liu, W. Feng, X. Xu and W. Yao, *Phys. Rev. Lett.*, 2012, **108**, 196802.

6 M. M. Ugeda, A. J. Bradley, S.-F. Shi, F. H. da Jornada, Y. Zhang, D. Y. Qiu, W. Ruan, S.-K. Mo, Z. Hussain, Z.-X. Shen, F. Wang, S. G. Louie and M. F. Crommie, *Nat. Mater.*, 2014, **13**, 1091–1095.

7 J. R. Schaibley, H. Yu, G. Clark, P. Rivera, J. S. Ross, K. L. Seyler, W. Yao and X. Xu, *Nat. Rev. Mater.*, 2016, **1**, 16055.

8 J. M. Lu, O. Zheliuk, I. Leermakers, N. F. Q. Yuan, U. Zeitler, K. T. Law and J. T. Ye, *Science*, 2015, **350**, 1353–1357.

9 B. Radisavljevic, A. Radenovic, J. Brivio, V. Giacometti and A. Kis, *Nat. Nanotechnol.*, 2011, **6**, 147–150.

10 S. Manzeli, D. Ovchinnikov, D. Pasquier, O. V. Yazyev and A. Kis, *Nat. Rev. Mater.*, 2017, **2**, 17033.

11 H. Zhang, C. Bao, Z. Jiang, K. Zhang, H. Li, C. Chen, J. Avila, Y. Wu, W. Duan, M. C. Asensio and S. Zhou, *Nano Lett.*, 2018, **18**, 4664–4668.

12 H. Li, U. Kumar, K. Sun and S.-Z. Lin, *Phys. Rev. Res.*, 2021, **3**, L032070.

13 H. Park, J. Cai, E. Anderson, Y. Zhang, J. Zhu, X. Liu, C. Wang, W. Holtzmann, C. Hu, Z. Liu, T. Taniguchi, K. Watanabe, J.-H. Chu, T. Cao, L. Fu, W. Yao, C.-Z. Chang, D. Cobden, D. Xiao and X. Xu, *Nature*, 2023, **622**, 74–79.

14 Y. Zeng, Z. Xia, K. Kang, J. Zhu, P. Knüppel, C. Vaswani, K. Watanabe, T. Taniguchi, K. F. Mak and J. Shan, *Nature*, 2023, **622**, 69–73.

15 J. Cai, E. Anderson, C. Wang, X. Zhang, X. Liu, W. Holtzmann, Y. Zhang, F. Fan, T. Taniguchi, K. Watanabe, Y. Ran, T. Cao, L. Fu, D. Xiao, W. Yao and X. Xu, *Nature*, 2023, **622**, 63–68.

16 F. Xu, Z. Sun, T. Jia, C. Liu, C. Xu, C. Li, Y. Gu, K. Watanabe, T. Taniguchi, B. Tong, *et al.*, *Phys. Rev. X*, 2023, **13**, 031037.

17 F. Wu, T. Lovorn, E. Tutuc, I. Martin and A. H. MacDonald, *Phys. Rev. Lett.*, 2019, **122**, 086402.

18 T. Devakul, V. Crépel, Y. Zhang and L. Fu, *Nat. Commun.*, 2021, **12**, 6730.

19 V. Crépel and L. Fu, *Phys. Rev. B*, 2023, **107**, L201109.

20 Z. Tao, B. Shen, W. Zhao, N. C. Hu, T. Li, S. Jiang, L. Li, K. Watanabe, T. Taniguchi, A. H. MacDonald, J. Shan and K. F. Mak, *Nat. Nanotechnol.*, 2024, **19**, 28–33.

21 W. Zhao, K. Kang, Y. Zhang, P. Knüppel, Z. Tao, L. Li, C. L. Tschirhart, E. Redekop, K. Watanabe, T. Taniguchi, A. F. Young, J. Shan and K. F. Mak, *Nat. Phys.*, 2024, **20**, 275–280.

22 T. Li, S. Jiang, B. Shen, Y. Zhang, L. Li, Z. Tao, T. Devakul, K. Watanabe, T. Taniguchi, L. Fu, J. Shan and K. F. Mak, *Nature*, 2021, **600**, 641–646.

23 C. Nayak, S. H. Simon, A. Stern, M. Freedman and S. Das Sarma, *Rev. Mod. Phys.*, 2008, **80**, 1083–1159.

24 T. T. Pham, R. Castelino, A. Felten and R. Sporken, *Appl. Surf. Sci.*, 2020, **523**, 146428.

25 Y. Huang, Y.-H. Pan, R. Yang, L.-H. Bao, L. Meng, H.-L. Luo, Y.-Q. Cai, G.-D. Liu, W.-J. Zhao, Z. Zhou, L.-M. Wu, Z.-L. Zhu, M. Huang, L.-W. Liu, L. Liu, P. Cheng, K.-H. Wu, S.-B. Tian, C.-Z. Gu, Y.-G. Shi, Y.-F. Guo, Z. G. Cheng, J.-P. Hu, L. Zhao, G.-H. Yang, E. Sutter, P. Sutter, Y.-L. Wang, W. Ji, X.-J. Zhou and H.-J. Gao, *Nat. Commun.*, 2020, **11**, 2453.

26 Y. Zhang, M. M. Ugeda, C. Jin, S.-F. Shi, A. J. Bradley, A. Martín-Recio, H. Ryu, J. Kim, S. Tang, Y. Kim, B. Zhou, C. Hwang, Y. Chen, F. Wang, M. F. Crommie, Z. Hussain, Z.-X. Shen and S.-K. Mo, *Nano Lett.*, 2016, **16**, 2485–2491.

27 G. Liu, G. Wang, Y. Zhu, H. Zhang, G. Zhang, X. Wang, Y. Zhou, W. Zhang, H. Liu, L. Zhao, J. Meng, X. Dong, C. Chen, Z. Xu and X. J. Zhou, *Rev. Sci. Instrum.*, 2008, **79**, 023105.

28 P. E. Blöchl, *Phys. Rev. B:Condens. Matter Mater. Phys.*, 1994, **50**, 17953–17979.

29 G. Kresse and D. Joubert, *Phys. Rev. B:Condens. Matter Mater. Phys.*, 1999, **59**, 1758–1775.

30 G. Kresse and J. Furthmüller, *Comput. Mater. Sci.*, 1996, **6**, 15–50.

31 G. Kresse and J. Furthmüller, *Phys. Rev. B:Condens. Matter Mater. Phys.*, 1996, **54**, 11169.

32 K. Lee, É. D. Murray, L. Kong, B. I. Lundqvist and D. C. Langreth, *Phys. Rev. B:Condens. Matter Mater. Phys.*, 2010, **82**, 081101.

33 M. Dion, H. Rydberg, E. Schröder, D. C. Langreth and B. I. Lundqvist, *Phys. Rev. Lett.*, 2004, **92**, 246401.

34 J. Klimeš, D. R. Bowler and A. Michaelides, *Phys. Rev. B: Condens. Matter Mater. Phys.*, 2011, **83**, 195131.

35 J. Hong, Z. Hu, M. Probert, K. Li, D. Lv, X. Yang, L. Gu, N. Mao, Q. Feng, L. Xie, *et al.*, *Nat. Commun.*, 2015, **6**, 6293.

36 J. Qiao, X. Kong, Z.-X. Hu, F. Yang and W. Ji, *Nat. Commun.*, 2014, **5**, 4475.

37 J. Qiao, Y. Pan, F. Yang, C. Wang, Y. Chai and W. Ji, *Sci. Bull.*, 2018, **63**, 159–168.

38 Z.-X. Hu, X. Kong, J. Qiao, B. Normand and W. Ji, *Nanoscale*, 2016, **8**, 2740–2750.

39 Y. Zhao, J. Qiao, P. Yu, Z. Hu, Z. Lin, S. P. Lau, Z. Liu, W. Ji and Y. Chai, *Adv. Mater.*, 2016, **28**, 2399–2407.

40 Y. Zhao, J. Qiao, Z. Yu, P. Yu, K. Xu, S. P. Lau, W. Zhou, Z. Liu, X. Wang, W. Ji, *et al.*, *Adv. Mater.*, 2017, **29**, 1604230.

41 J. P. Perdew, K. Burke and M. Ernzerhof, *Phys. Rev. Lett.*, 1996, **77**, 3865.

42 C. Ruppert, B. Aslan and T. F. Heinz, *Nano Lett.*, 2014, **14**, 6231–6236.

43 See ESI at https://doi.org/10.1039/d4nr05191b for the details.†

44 T. Böker, R. Severin, A. Müller, C. Janowitz, R. Manzke, D. Voß, P. Krüger, A. Mazur and J. Pollmann, *Phys. Rev. B: Condens. Matter Mater. Phys.*, 2001, **64**, 235305.

45 Y. Zhang, T.-R. Chang, B. Zhou, Y.-T. Cui, H. Yan, Z. Liu, F. Schmitt, J. Lee, R. Moore, Y. Chen, H. Lin, H.-T. Jeng, S.-K. Mo, Z. Hussain, A. Bansil and Z.-X. Shen, *Nat. Nanotechnol.*, 2014, **9**, 111–115.

46 J. A. Miwa, S. Ulstrup, S. G. Sørensen, M. Dendzik, A. G. Čabo, M. Bianchi, J. V. Lauritsen and P. Hofmann, *Phys. Rev. Lett.*, 2015, **114**, 046802.

47 M. Dendzik, M. Michiardi, C. Sanders, M. Bianchi, J. A. Miwa, S. S. Grønborg, J. V. Lauritsen, A. Bruix, B. Hammer and P. Hofmann, *Phys. Rev. B:Condens. Matter Mater. Phys.*, 2015, **92**, 245442.

48 T. T. Han, L. Chen, C. Cai, Z. G. Wang, Y. D. Wang, Z. M. Xin and Y. Zhang, *Phys. Rev. Lett.*, 2021, **126**, 106602.

49 C. Robert, R. Picard, D. Lagarde, G. Wang, J. P. Echeverry, F. Cadiz, P. Renucci, A. Högele, T. Amand, X. Marie, I. C. Gerber and B. Urbaszek, *Phys. Rev. B*, 2016, **94**, 155425.

50 N. Zibouche, A. Kuc, J. Musfeldt and T. Heine, *Ann. Phys.*, 2014, **526**, 395–401.

51 I. G. Lezama, A. Arora, A. Ubaldini, C. Barreteau, E. Giannini, M. Potemski and A. F. Morpurgo, *Nano Lett.*, 2015, **15**, 2336–2342.

52 S. Helmrich, R. Schneider, A. W. Achtstein, A. Arora, B. Herzog, S. M. de Vasconcellos, M. Kolarczik, O. Schöps, R. Bratschitsch, U. Woggon and N. Owschimikow, *2D Mater.*, 2018, **5**, 045007.

53 M. Kang, B. Kim, S. H. Ryu, S. W. Jung, J. Kim, L. Moreschini, C. Jozwiak, E. Rotenberg, A. Bostwick and K. S. Kim, *Nano Lett.*, 2017, **17**, 1610–1615.

54 S. B. Desai, G. Seol, J. S. Kang, H. Fang, C. Battaglia, R. Kapadia, J. W. Ager, J. Guo and A. Javey, *Nano Lett.*, 2014, **14**, 4592–4597.

55 W. Jin, P.-C. Yeh, N. Zaki, D. Zhang, J. T. Sadowski, A. Al-Mahboob, A. M. van der Zande, D. A. Chenet, J. I. Dadap, I. P. Herman, P. Sutter, J. Hone and R. M. Osgood, *Phys. Rev. Lett.*, 2013, **111**, 106801.

56 H. Yuan, Z. Liu, G. Xu, B. Zhou, S. Wu, D. Dumcenco, K. Yan, Y. Zhang, S.-K. Mo, P. Dudin, V. Kandyba, M. Yablonskikh, A. Barinov, Z. Shen, S. Zhang, Y. Huang, X. Xu, Z. Hussain, H. Y. Hwang, Y. Cui and Y. Chen, *Nano Lett.*, 2016, **16**, 4738–4745.

57 W. Zhao, Z. Ghorannevis, L. Chu, M. Toh, C. Kloc, P.-H. Tan and G. Eda, *ACS Nano*, 2013, **7**, 791–797.

58 J. Kutrowska-Girzycka, E. Zieba-Ostój, D. Biegańska, M. Florian, A. Steinhoff, E. Rogowicz, P. Mrowiński, K. Watanabe, T. Taniguchi, C. Gies, S. Tongay, C. Schneider and M. Syperek, *Appl. Phys. Rev.*, 2022, **9**, 041410.

59 B. Han, J. M. Fitzgerald, L. Lackner, R. Rosati, M. Esmann, F. Eilenberger, T. Taniguchi, K. Watanabe, M. Syperek, E. Malic and C. Schneider, *Phys. Rev. Lett.*, 2025, **134**, 076902.

60 I. V. Lebedeva, A. S. Minkin, A. M. Popov and A. A. Knizhnik, *Phys. E*, 2019, **108**, 326–338.

61 A. H. Reshak and M. Jamal, *J. Alloys Compd.*, 2012, **543**, 147–151.

62 K. F. Mak, C. Lee, J. Hone, J. Shan and T. F. Heinz, *Phys. Rev. Lett.*, 2010, **105**, 136805.

63 G. Froehlicher, E. Lorchat and S. Berciaud, *Phys. Rev. B*, 2016, **94**, 085429.

64 J. M. Riley, F. Mazzola, M. Dendzik, M. Michiardi, T. Takayama, L. Bawden, C. Granerød, M. Leandersson, T. Balasubramanian, M. Hoesch, T. K. Kim, H. Takagi, W. Meevasana, P. Hofmann, M. S. Bahramy, J. W. Wells and P. D. C. King, *Nat. Phys.*, 2014, **10**, 835–839.

65 Y. Zhang, H. Li, H. Wang, R. Liu, S.-L. Zhang and Z.-J. Qiu, *ACS Nano*, 2015, **9**, 8514–8519.

66 K. F. Mak, K. He, J. Shan and T. F. Heinz, *Nat. Nanotechnol.*, 2012, **7**, 494–498.

67 P. Eickholt, C. Sanders, M. Dendzik, L. Bignardi, D. Lizzit, S. Lizzit, A. Bruix, P. Hofmann and M. Donath, *Phys. Rev. Lett.*, 2018, **121**, 136402.

68 S. Mahatha and K. S. Menon, *J. Electron Spectrosc. Relat. Phenom.*, 2014, **193**, 43–47.

69 A. Bruix, J. A. Miwa, N. Hauptmann, D. Wegner, S. Ulstrup, S. S. Grønborg, C. E. Sanders, M. Dendzik, A. Grubišć Čabo, M. Bianchi, J. V. Lauritsen, A. A. Khajetoorians, B. Hammer and P. Hofmann, *Phys. Rev. B*, 2016, **93**, 165422.